Colloid Polym Sci 279: 348–360 (2001)
© Springer-Verlag 2001
ORIGINAL CONTRIBUTION

Y. Sugiura
M. Matsuo

Description of the state of deformation of ethylene–tetrafluoroethylene alternating copolymer films estimated by using a model proposed in terms of orientation of crystallites within a rod

Received: 28 April 2000
Accepted: 30 September 2000

Y. Sugiura · M. Matsuo (✉)
Department of Textile Apparel Science
Faculty of Human Life and Environment
Nara Women's University
Nara 630, Japan
E-mail: matsuo@nara-wu.ac.jp

Abstract To study the deformation mechanism of ethylene–tetrafluoroethylene alternating copolymer films caused by elongation, a model relating crystal orientation to the orientation of the rods was proposed. The orientation distribution of crystallites within the rod was given as the correlation with the rod orientation. The distribution functions of a given reciprocal lattice vector of the crystal plane were derived from the two functions of the crystallites and of rods with several parameters representing the orientation of rods and the rotation of crystallites within a rod. By choosing suitable values of the parameters, the calculated functions were in good agreement with the results of X-ray diffraction experiments. From the values of the parameters to give the best fit between calculated and observed results, it turned out that the characteristic orientation of the *c*-axis is mainly due to the preferential orientation of the rod with respect to a stretching direction and is hardly affected by the rotation of crystallites within the rod. Using the two orientation functions concerning rods and crystallites, Hv light scattering was formulated by introducing an interparticle interference effect of the rods. The calculated results assumed the characteristic profile of the observed patterns as the superposition of broadleaf lobes and a sharp pattern of streaks.

Key words Ethylene-tetrafluoroethylene alternating copolymer films · Orientation distribution of crystallites · Rod orientation · Hv light scattering · Interparticle interference effect

Introduction

Several studies on the crystal structure for ethylene–tetrafluoroethylene (ETFE) have been reported in the literature [1–11]. From detailed work, it is accepted that the unit cell for ETFE is an orthorhombic form [1, 2], and a thermal reversible transition occurs in a wide range from 0 to 100 °C [3–8]. Tanigami et al. [2] pointed out that the dimensions of the unit cell of ETFE are $a = 8.57$ Å, $b = 11.2$ Å and $c = 5.04$ Å, and the crystal structure which has been assumed to be pseudohexagonal is indeed orthorhombic. They concluded that four zigzag chains pack in the unit cell and that the lateral packing mode is similar to that of orthorhombic polyethylene.

At low temperatures the crystal unit of ETFE shows an orthorhombic form and is transformed to a hexagonal form with increasing temperature [3, 5–7]. Tanigami et al. [3] suggested that the transition was an order–disorder transition, associated with rotational motion around the chain axis like for polyethylene.

Detailed treatments of the deformation mechanism of ETFE with different side chain modifications were investigated by Pieper et al. [11] in terms of the second-order orientation factors of the chain segments in the amorphous layers and the crystallographic axes. They demonstrated that the crystal orientation is independent of the side chain modifications. Furthermore, they measured the temperature dependence of both the mean lattice constant and the mean extension of the coherent scattering domains by using synchrotron radiation and pointed out that the anomaly of these parameters at about 100 °C is attributed to a transition of the crystal structure.

On the basis of reported characteristics of ETFE crystallites, this article deals with the orientation of ETFE crystallites. Actually, there has been no report for crystal orientation discussed in relation to the orientation of a rodlike structure, although detailed analysis of crystal orientation has been carried out for polyethylene films with spherulites [12–14]. The quantitative orientation behavior of crystallites has been estimated in terms of orientation distribution functions of the reciprocal lattice vectors of several crystal planes [12–14]. In accordance with this concept, the observed functions were compared with the ones calculated on the basis of a model relating the crystal orientation to the orientation of rods confirmed by small-angle light scattering under a Hv polarization condition. In this model system, the distribution function of crystallites within the rod is assumed to be an orientation function of the rods. By using the orientation function of the crystallites and that of the rods, Hv light scattering patterns are calculated by the introduction of an interparticle interference effect of the rods [15, 16]. The theoretical patterns are estimated in comparison with observed ones.

Experimental

Pellets of ETFE whose commercial name is Neoflon, EP-521, were obtained through the courtesy of Daikin Co. According to available data from this company, the melt index is 12 g/10 min at 297 °C. The molecular weight is in the range 2–3 × 10^5. The ratio of ethylene (ET) and tetrafluoroethylene (TFE), however, is not open to the public. A torque rheometer, Haake Rheocord 90, was employed to knead the pellets. The mixing was done by rotating at 60 rpm at a temperature of 260 °C for 5 min under nitrogen flow. All mixtures were pressed at 260 °C under 19.6 MPa for 5 min and then the resultant film was quenched in water. The film was cut into strips, which were elongated to the desired draw ratio at 130 °C under nitrogen.

The density of the specimens was measured using a pycnometer with methyl iodide-carbon and tetrachloride as reference liquids.

The complex dynamic tensile modulus function was measured at a frequency of 10 Hz over a temperature range from −150 to 200 °C. The length of the specimen between the jaws was about 40 mm and the width was 2 mm. The specimen was heated at a constant rate of 2 °C min^{-1}. The complex dynamic modulus was measured by imposing a small dynamic strain to ensure linear viscoelastic behavior of the specimen.

Light scattering patterns were obtained with a 3-mW He–Ne gas laser as the light source. Diffuse scattering was avoided by sandwiching the specimen between microcover glasses with a silicone immersion oil having a similar index of refraction.

The X-ray measurements were carried out with a 12-kW rotating-around Rigaku RDA-rA. The X-ray beam was monochromatized with a curved graphite monochromator using Cu Kα radiation at 200 mA and 40 kV. The wide-angle X-ray diffraction (WAXD) intensity distribution was measured by point focus at a step interval of 0.1° with a time interval of 40 s, in the desired range of twice the Bragg angle, $2\theta_B$. The diffraction beam was detected by a square slit of 1 mm × 1 mm.

To estimate the orientation distribution function of the reciprocal lattice vector of the crystal planes, the X-ray measurements were performed using a horizontal scanning type goniometer over a range of $2\theta_B$, from 12 to 24° and from 70 to 81°. In this condition, the tilting of the specimen to estimate the orientation of the (*hkl*) reflections was carried out by rotating about the film normal direction at 2–5° intervals in the range from 0 to 90°. After correcting for air scattering, background noise, polarization, absorption and the amorphous contribution, the intensity distribution was obtained as a function of a given rotating angle of θ_j. The intensity curve thus obtained was assumed to be the contribution of the intensity form the crystalline phase. The intensity curve, $I_{cry}(2\theta_B)$, for the (004) plane showed a symmetric form given by a Lorentzian function of $2\theta_B$. In contrast, the intensity curve having a peak around 19° showed an overlapping diffraction from the (120), (200) and (001) planes which can be postulated from the crystal unit cell proposed by Tanigami et al. [2]. The curve could not be separated into the contributions from the individual crystal planes by assuming a Lorentzian function because the reflections from the three crystal planes were located very close to each other. The intensity distribution, $I_j(\theta_j)$, can be determined for the respective *j*th plane, and the orientation distribution function of the *j*th reciprocal lattice vector may be given by

$$2\pi q_j(\cos\theta_j) = \frac{I(\theta_j)}{\int_0^{\pi/2} I(\theta_j)\sin\theta_j \, d\theta_j} \quad . \tag{1}$$

Because of the difficulty of peak separation, the composed function $2\pi q_j(\cos\theta_j)$ includes the contribution of several planes as follows:

$$2\pi q_j(\cos\theta_j) = 2\pi \sum_{i=1}^{N_i} C_{ji} q_{ji}(\cos\theta_j) \quad . \tag{2}$$

The concept underlying Eq. (2) was first presented by Roe and Krigbaum [17, 18]. N_i is the number of the *j*th superposed peaks and C_{ji} is the relative (normalized) weight for the vector r_{ji}. The values of C_{ji} are given by

$$C_{ji} = \frac{F_j}{\sum_{i=1}^{N_i} F_{ji}} \quad , \tag{3}$$

where F_j is the structure factor of the *j*th crystal plane. Equation (2) was applied to an overlapped distribution function, $2\pi q_j(\cos\theta_j)$, of the (120), (200) and (001) planes around $2\theta_B = 19°$.

The second-order orientation factor F_{20}^j for the *j*th plane is given by

$$F_{20}^j = \int_0^{\pi} \frac{1}{2}(3\cos^2\theta_j - 1) q_j(\cos\theta_j)\sin\theta_j \, d\theta_j \quad . \tag{4}$$

Incidentally, the orientation of the crystallites was confirmed to be oriented randomly around the stretching direction by the circular rings of the diffraction pattern (end view).

Results and discussion

The changes in the density, the birefringence and the second-order orientation factor of the *c*-axis (the crystal chain axis) with draw ratio are shown in Table 1. For reproducibility, the measurements at a given draw ratio were carried out several times and the average value is listed. The careful measurements suggest a very slight increase in density with draw ratio due to oriented crystallization. The corresponding birefringence and the second-order orientation factor of the *c*-axis increase with draw ratio, indicating a significant molecular orientation with respect to the stretching direction.

Table 1 Change in density, birefringence and second-order orientation factors of the *c*-axis with increasing draw ratio

Draw ratio	1	1.5	2	3	4	5	6
Density	1.727	1.728	1.728		1.729		1.73
Birefringence ($\times 10^{-3}$)		17.5	30.9	38.2	42.4	50.0	51.6
Second-order orientation factor		0.261	0.551	0.729	0.879	0.919	0.922

The WAXD intensity distributions of undrawn and drawn films are shown in Fig. 1. Each curve of the two samples shows an asymmetric single peak around $2\theta_B = 19°$ in spite of superposed reflections from the (120), (200) and (001) planes. This measurement was done to make clear the crystal form of ETFE in order to estimate the orientation of crystallites under elongation. The peak position around 19° shifted toward a lower angle of $2\theta_B$ and the curve became sharper with draw ratio. This asymmetric peak of ETFE has been observed for the drawn films in previous work [1–3] and it suggests that ETFE has a pseudohexagonal structure. According to Tanigami et al. [2], the asymmetry was interpreted as a doublet character of the peak. They concluded that the crystal structure of ETFE, which has been considered to be pseudohexagonal, is indeed orthorhombic having the paracrystalline disorder in the lateral packing of the chain [2]. In the present work, the change in the peak position between drawn and undrawn films indicated the expansion of the lattice space, which might be influenced by the stress and the thermal treatment concerning the sample preparation.

The influences of thermal history and stress on the ETFE crystallites were examined to obtain more detailed information with regard to the crystal structure within the present specimens, since ETFE is well known to invoke the crystal transition from an orthorhombic unit to a hexagonal one with temperature reversibly. In the present work, the undrawn films were subjected to heating cycles from room temperature (27 °C) to 150 °C followed by cooling to room temperature under stress or no stress. The results are shown in Fig. 2. The open and closed circles indicate the situation under no stress and with an applied external stress of 3 MPa, respectively. In the heating process, the peak position shifted toward a lower angle of $2\theta_B$ with increasing temperature irrespective of the stress.

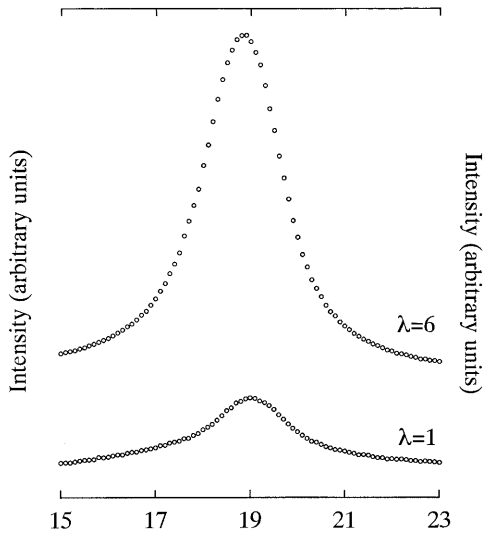

Fig. 1 X-ray diffraction profiles of drawn ($\lambda = 6$) and undrawn films

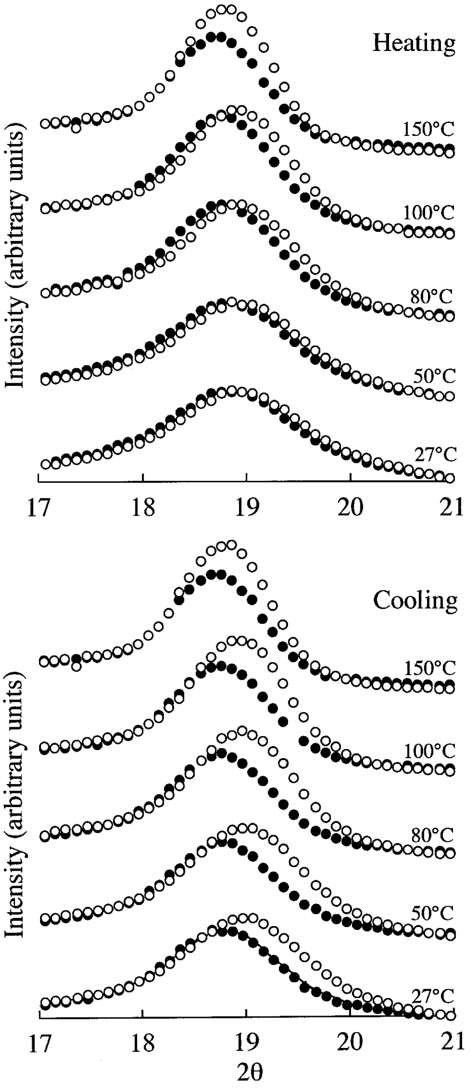

Fig. 2 *Top*: X-ray diffraction intensity distribution of the undrawn film in the heating process. *Bottom*: X-ray diffraction intensity distribution of the undrawn film in the cooling process. *Open circles*: under no stress; *filled circles*: under a stress of 3 MPa

This indicates the significant expansion of the lattice space of the (120) and (200) planes at elevated temperature. In the cooling process, the diffraction peak under no stress shifted reversibly to the original position; however, the crystal transition did not occur reversibly under stress. Interestingly, the peak position did not return anymore, even when the applied stress was removed after the thermal cycle measurements.

Recently, D'Aniello et al. [7] reported the influence of the thermal history on the polymorphic behavior of ETFE. According to their experiment, the specimen quenched from the melt tends to a better developed orthorhombic form and the reversibility of the thermal transition is incomplete in the case where the specimen is cooled slowly. Although the specimen in Fig. 2 was cooled slowly, a reversible change in the peak position could be observed under no stress, but under stress it was not so. The intensity curves drawn as open circles are completely in accord but the curves drawn as solid circles did not overlap. It is our understanding that the change in the X-ray diffraction peak was influenced by stress over temperature.

To facilitate an understanding of the crystal transition, the temperature dependence of the storage and loss moduli was measured for the undrawn ($\lambda = 1$) and drawn films ($\lambda = 6$). The results are shown in Fig. 3. The loss modulus for the undrawn film shows a very broad peak in the temperature range of 0–100 °C. The broad peak has been reported to be classified into two mechanisms, α' and α [19, 20]. The α' mechanism is related to the crystal transition from an orthorhombic to a pseudohexagonal unit or from a pseudohexagonal unit to a hexagonal unit, while the a mechanism is related to a complete crystal transformation at about 90 °C, assigned to the glass transition [20, 21]. If this is the case, the transition must be detected as a small change in the X-ray diffraction. As discussed already, however, such a transition could not be observed by the diffraction peaks around $2\theta_B = 19°$.

As discussed later, the existence of superstructure within the ETFE film was confirmed by small-angle light scattering under Hv polarization conditions as has been confirmed for polyethylene, and the temperature dependence of the loss modulus of ETFE [20, 21] is similar to that of polyethylene having α, β and γ dispersions [22]. Therefore, as one of the possibilities, the α' and α mechanisms of ETFE are thought to correspond to the α_1 and α_2 mechanisms of polyethylene, respectively [23, 24]. Namely, the former is associated with the grain boundary phenomenon concerning deformation and/or rotation of crystallites within a various media and the latter is associated with the crystal disordering transition due to the onset of torsional oscillation of the polymer chain within the crystal lattice [25, 26].

Through a series of experimental results presented here, it may be expected that the ETFE crystal unit is represented as a pseudohexagonal structure. In a previous report [2], as stated earlier, it was concluded that the pseudohexagonal structure of ETFE seems to be based on orthorhombic packing. We also treated the specimens as an orthorhombic unit cell with $a = 8.57$ Å, $b = 11.2$ Å and $c = 5.04$ Å proposed by Tanigami et al. [2] to study the orientation of ETFE crystallites as a function of elongation. Using the orthorhombic unit cell, the orientation of ETFE crystallites was estimated to explain the sequence of deformation by the existence of superstructure. As for the molecular orientation of ETFE, a detailed analysis was done by Pieper et al. [11] in terms of the second-order orientation factor. The orientation factor of the amorphous chain segments was determined from the separated amorphous halo of the intensity distribution. The orientation distribution of the three principal crystallographic axes was obtained from the analysis of the (*hk*0) reflections. They pointed out that the difference of the *a*- and *b*-axis orientations is due to the existence of a lamellar structure analogous to polyethylene and that the orientational degree of the *c*-axis is lower than that of polyethylene.

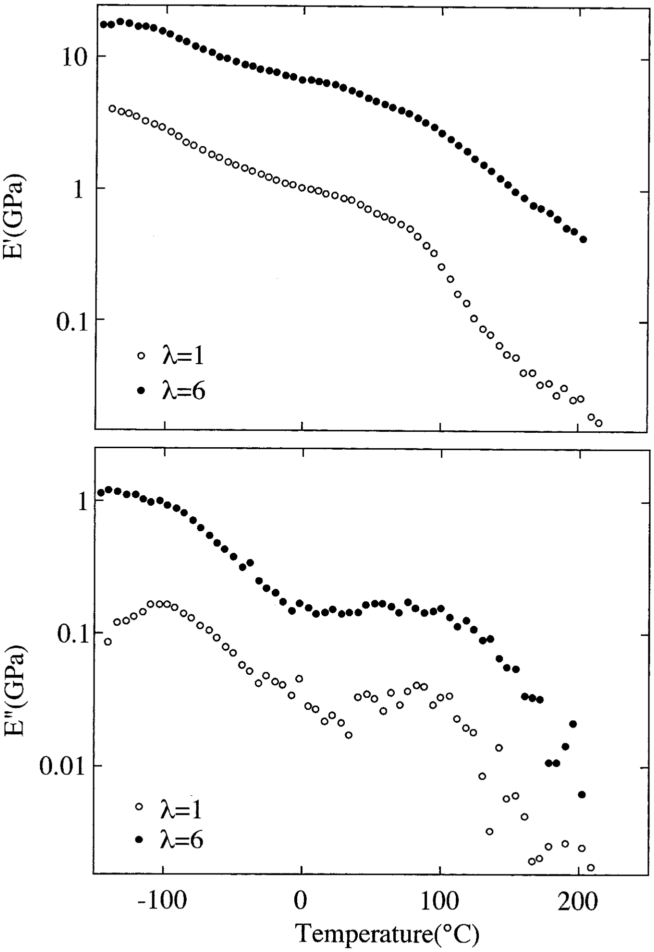

Fig. 3 Temperature dependence of the storage and loss moduli of the undrawn and drawn films ($\lambda = 6$)

Instead of the second-order orientation factor, this treatment was done in terms of the orientation distribution functions of the reciprocal lattice vector by using the overlapped peak of the (120), (200) and (001) planes appearing around $2\theta_{\mathrm{B}} = 19°$ and the single peak of the (004) plane around $2\theta_{\mathrm{B}} = 75°$. To propose a model relating the crystal orientation to the orientation of the superstructure, light scattering patterns under Hv polarization conditions were observed [27, 28]. The changes in the patterns with draw ratio are shown in Fig. 4. The scattering from an undrawn film displays an indistinct circular pattern, in which the intensity decreased continuously with increasing scattering angle. This is typical of the scattering from a system composed of a random array of crystallites that are small compared with the wavelength of the incident beam. Elongation causes the development of a clear X-type pattern whose lobes are extended in the horizontal direction, indicating the growth of the rods and the preferential orientation of the rods with respect to the stretching direction. Optical micrographs (cross-polarized) at $\lambda = 4$ and 6 suggest that the optical axes are oriented parallel to the rod axis in an undeformed state. Unfortunately the micrographs were too indistinct to be shown as figures because of the thick films. The sharp streaks in the horizontal direction in the Hv pattern at $\lambda = 1.5$–3 have been observed for oriented crystalline films with rods or sheaflike textures such as poly(ethylene terephthalate) [29], hydroxypropylcellulose [16] and poly(tetramethylene oxide)–poly(tetramethylene terephthalate) block polymer [15]. They are probably thought to be attributed as an interparticle interference effect of the rods, which is discussed later.

The question can be raised whether these sharp streaks can be associated with a biaxial component of stretching that can arises from one-dimensional stretching of a sample of small length-to-width ratio. The dimensional changes with draw ratio indicate that when the specimen was drawn uniaxially up to λ_3, the value of λ_1, the draw ratio being in the thickness direction, is close to that of λ_2, the draw ratio being in the transverse direction and $\lambda_1\lambda_2\lambda_3$ becomes unity. Of course, the X-ray diffraction pattern (end views) showed circular rings, as discussed before.

The geometrical interactions of three Cartesian systems, 0-$X_1X_2X_3$, 0-$V_1V_2V_3$ and 0-$U_1U_2U_3$, fixed within the bulk specimen, rod and crystallite, respectively, are shown in Tables 2 and 3. The directions of the coordinate axes of each Cartesian system are given in Table 2, the Euler angles of coordinate transformation between the three Cartesian systems are given in Table 4 and two sets of the polar angle and azimuthal angles of a given reciprocal lattice vector of the crystallite with respect to the three Cartesian systems are given in Table 3. Within the ETFE rod, it is assumed that the *c*-axis orients predominantly in the direction of the rod axis in an undeformed state and that the crystallites within a rod are connected, more or less, to each other by "tie-chain molecules". On uniaxial stretching, the rod may be oriented predominantly in a preferred direction, which depends on the draw ratio, without changing its length. In this process, it is expected that the rotation of a rod around its own axis is not random but takes a characteristic mode; however, we do not know the deformation mechanism in detail. Accordingly, the orientation of rods may be formulated by the orientation of the Cartesian system 0-$V_1V_2V_3$ with respect to the Cartesian system 0-$X_1X_2X_3$ by using parameters characterizing two typical rotations as follows:

$$\omega(\theta', \eta') = \frac{C_0}{8\pi^2}\omega(\theta')\left[1 + \sigma_1(\lambda - 1)\cos^{2\mathrm{JA}}\eta' + \sigma_2(\lambda - 1)\sin^{2\mathrm{JA}}\eta'\right] \tag{5}$$

and

$$\omega(\theta') = \left(\frac{\cos^2\theta'\left(2\cos^2\theta_0 - \cos^2\theta'\right)}{\cos^4\theta_0} + \mathrm{fr}\right)^{2\mathrm{JB}} . \tag{6}$$

The second term on the right-hand side of Eq. (5) represents the rotational mode of the rod axis (V_3 axis) to allow the preferential orientation of the rod normal direction (V_1 axis) with respect to the 0-X_3V_3 plane, while the third term is a rotational mode taking the preferential orientation of the V_1 axis perpendicular to the 0-X_3V_3 plane. σ_1 and σ_2 are parameters characterizing the ease of the former and latter rotational modes, respectively, and JA represents their sharpness. In Eq. (6), θ_0 is the angle between the preferred direction and the stretching direction, in which the orientation distribution of the rod axes within a deformed film has the maximum value at θ_0. JB is a parameter characterizing the sharpness of the orientation of the rod axis and fr is a random parameter to moderate the sharpness of the orientation function of the rod axis. At $\mathrm{fr} = 0$, $\mathrm{JB} = 0$ means the random orientation of the rod axis with respect to the stretching direction, while $\mathrm{JB} = 8$ means the perfect orientation in the direction of θ_0. C_0 is a normalization constant defined by

$$\int_0^{2\pi}\int_0^{2\pi}\int_0^{\pi}\omega(\theta', \eta')\sin\theta'\mathrm{d}\theta'\mathrm{d}\phi'\mathrm{d}\eta' = 1 . \tag{7}$$

The orientation of the crystallites within the rod can be represented by the orientation of the Cartesian coordi-

$$q(\alpha, \beta, \gamma) = \frac{Q_0}{8\pi^2}\left[\begin{array}{l}\cos^{2\mathrm{JG}}\beta\cos^{2\mathrm{JC}}\alpha\cos^{2\mathrm{JD}}\gamma \\ +\sigma_3(\lambda_1 - 1)\left(\sin^4\theta' - \cos^4\beta + 2\cos^2\theta'\cos^2\beta\right)\cos^{2\mathrm{JE}}\alpha\cos^{2\mathrm{JF}}\gamma\end{array}\right] . \tag{8}$$

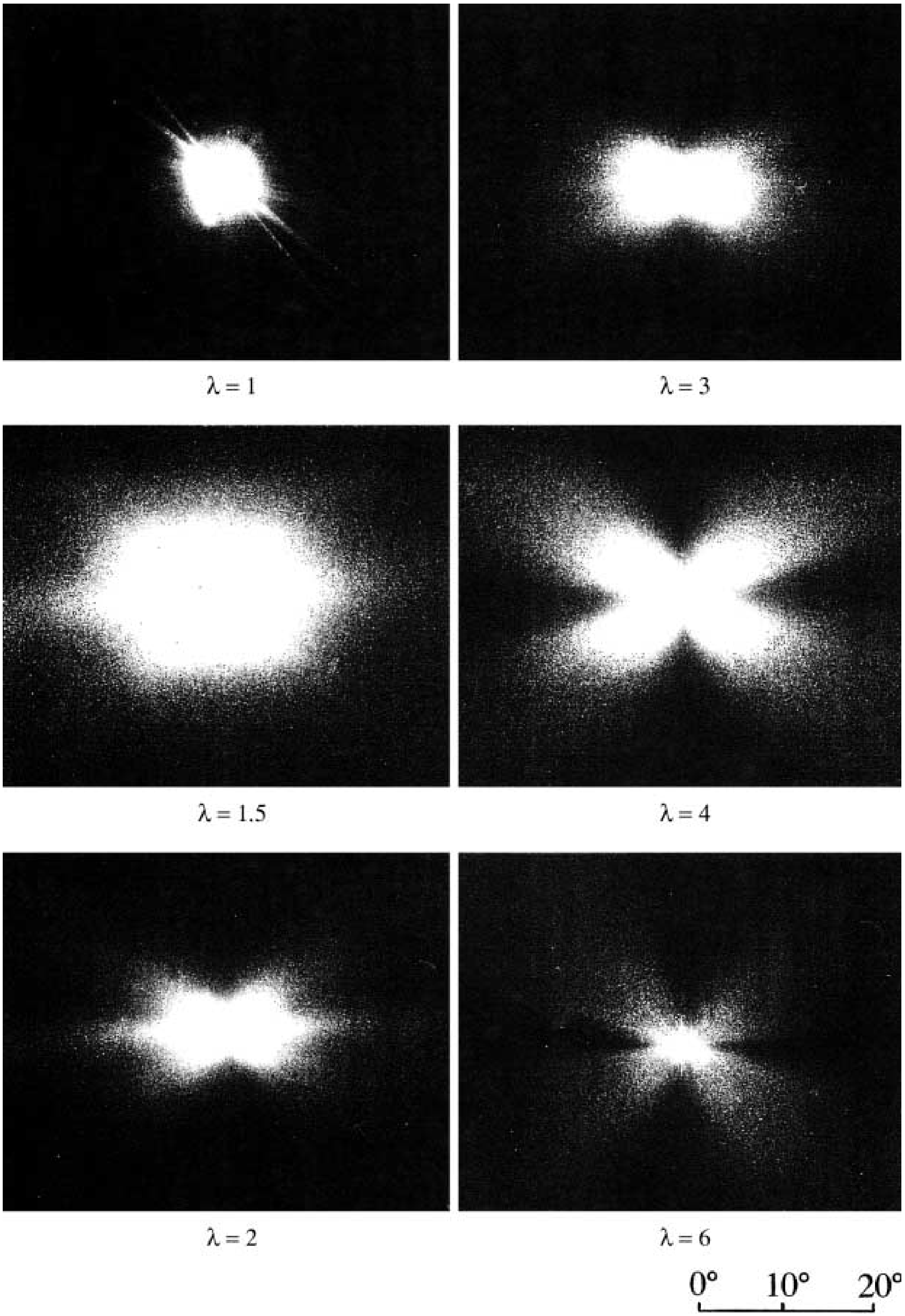

Fig. 4 Hv light scattering patterns from the films with the draw ratios indicated

nate 0-$U_1U_2U_3$ with respect to the Cartesian coordinate 0-$V_1V_2V_3$. The corresponding distribution function may be formulated as follows:
In the undeformed state ($\lambda = 1$), Eq. (8) reduces to

$$q(\alpha, \beta, \gamma) = \frac{Q_0}{8\pi^2}\left[\cos^{2JG}\beta \cos^{2JC}\alpha \cos^{2JD}\gamma\right] \ . \tag{9}$$

Q_0 is a normalization constant defined by

$$\int_0^{2\pi}\int_0^{2\pi}\int_0^{\pi} q(\alpha, \beta, \gamma) \sin\beta \, d\beta \, d\alpha \, d\gamma = 1 \ . \tag{10}$$

Thus Q_0 contains θ' terms in a deformed state and consequently Eq. (8) becomes somewhat complicated to

Table 2 Direction of coordinate axes

Coordinate system	Direction of coordinate of X_i, V_i and U_i axes	
	$i = 1$	$i = 3$
$0\text{-}X_1X_2X_3$	Normal to film surface	Stretching direction of film specimen
$0\text{-}V_1V_2V_3$	Normal to rod surface containing $0V_2$ and $0V_3$	Rod axis
$0\text{-}U_1U_2U_3$	The *a*-axis of ethylene–tetrafluoroethylene crystallite	The *c*-axis of ethylene–tetrafluoroethylene crystallite

Table 3 Three sets of orientation angles of a given reciprocal lattice vector, $\mathbf{r}_j$

Reference coordinate	Polar and azimuthal angles of $\mathbf{r}_j$
$0\text{-}X_1X_2X_3$	θ_j, ϕ_j
$0\text{-}U_1U_2U_3$	Θ_j, Φ_j

Table 4 Euler angles of coordinate transformations

Reference coordinate	Euler angles	Oriented coordinates
$0\text{-}X_1X_2X_3$	ϕ', θ', η'	$0\text{-}V_1V_2V_3$
$0\text{-}V_1V_2V_3$	α, β, γ	$0\text{-}U_1U_2U_3$

perform numerical calculations for obtaining $2\pi q_j(\cos\theta_j)$. Equation (9) is given as a function with a maximum value at $\alpha = 0°$, $\beta = 0°$ and $\gamma = 0°$. This reveals that when the values of JG, JC and JD are infinite, the *c*- and *a*-axes are oriented perfectly in the direction of the rod axis (V_3 axis) and the rod normal (V_1, thickness) direction, respectively, in an undeformed state.

In the deformed state, there is an additional component; namely, the second term on the right-hand side of Eq. (8) denotes the fraction of crystallites oriented predominantly parallel to the stretching direction. σ_3 is a parameter concerning the ratio of the undeformed and deformed fractions. The latter behavior is represented by the term $\sin^4\theta' - \cos^4\beta + 2\cos^2\theta'\cos^2\beta$, which has a maximum value for $\beta = \theta'$ irrespective of the polar angle of the rod orientation, θ'. This preferential orientation of the *c*-axis with respect to the stretching direction is assumed to take place because of straining of the tie-chain molecules by the rotation of crystallites around its own *b*-axis. This mode can be represented by the term, $\cos^{2JE}\alpha\cos^{2JF}\gamma$, in which the parameters JE and JF characterize the sharpness of the distribution with respect to the angles α and γ, respectively. Zero values of JE and JF mean that the orientation of the crystallites is random around the *c*-axis.

By using the results in the previous reports [30, 31], the orientation distribution function, $2\pi q_j(\cos\theta_j)$, of a given reciprocal lattice vector of the *j*th crystal plane can be determined by the following calculations.

$$Q_{\ell sn}(\theta') = \int_0^{2\pi}\int_0^{2\pi}\int_0^{\pi} q(\alpha,\beta,\gamma)P_{\ell sn}(\cos\beta) \times \cos s\alpha\cos n\gamma\sin\beta\,\mathrm{d}\beta\,\mathrm{d}\alpha\,\mathrm{d}\gamma \quad , \tag{11}$$

$$F'_{\ell sn} = \int_0^{2\pi}\int_0^{2\pi}\int_0^{\pi} \omega'(\theta',\eta')P_\ell^s(\cos\theta')Q_{\ell sn}(\theta') \times \cos s\eta'\,\mathrm{d}\theta'\,\mathrm{d}\eta'\,\mathrm{d}\phi' \quad , \tag{12}$$

$$F_{\ell 0n} = F'_{\ell 0n} + 2\sum_{s=2}^{\ell}\frac{(\ell-n)!}{(\ell+n)!}F'_{\ell sn} \tag{13}$$

$$F_{\ell 0}^i = F_{\ell 00}P_\ell(\cos\Theta_i) + 2\sum_{n=2}^{\ell}\frac{(\ell-n)!}{(\ell+n)!}F_{\ell 0n}P_\ell^n(\cos\Theta_i)\cos n\Phi_i \quad , \tag{14}$$

$$\begin{aligned}2\pi q_j(\cos\theta_j) &= 2\pi\sum_{i=1}^{N_i}C_{ji}q_{ji}(\cos\theta_j) \quad . \\ &= \sum_{i=1}^{N_i}C_{ji}\left(\frac{1}{2}+\sum_{\ell=2}^{\infty}\frac{2\ell+1}{2}F_{\ell 0}^{ji}P_i(\cos\theta_j)\right)\end{aligned} \tag{15}$$

However, $2\pi q_j(\cos\theta_j)$ for each crystal plane could not be observed because of the difficulty of peak separation for the (120), (200) and (001) planes. Actually, $2\pi q_j(\cos\theta_j)$ was estimated as an overlapped function, $2\pi q_{ji}(\cos\theta_{ji})$ [i = (120), (200) and (001)], by using Eq. (2). In addition to 12 parameters in Eqs. (5), (6) and (8), the best values of C_{ji} in Eq. (15) were also determined by the simplex method [32], which is a directed search method to obtain the object function on the basis of trial and error. The calculation was continued until the best fit was achieved within the capability of the simplex method.

Figure 5 shows the comparison between experimental results and calculated curves for the overlapped peak of the (120), (200) and (001) planes and for a single peak for the (004) plane and the values of 12 parameters in Eqs. (5), (6) and (8) to give the best fit are listed in Table 5. Here it should be noted that even $2\pi q_j(\cos\theta_j)$ of $\lambda = 4$ with a sharp distribution function shows positive values at most regions of the polar angle θ_j, because

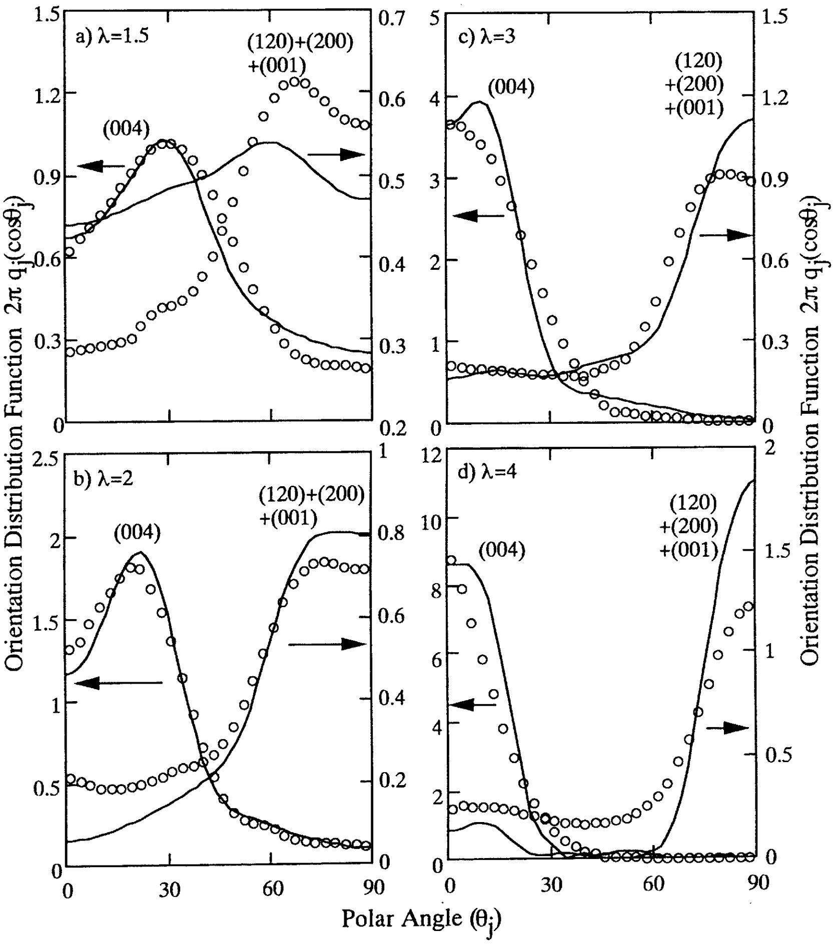

Fig. 5 Orientation distribution functions of the reciprocal lattice vectors estimated for the overlapped peak of the (120), (200) and (001) planes and for a single peak of the (004) plane. *Circular plot*: experimental results; *solid curve*: theoretical results

Table 5 Proper combination of values of the parameters in Eqs. (5), (6) and (8)

Draw ratio	θ_0	fr	σ_1	σ_2	σ_3	JA	JB	JC	JD	JE	JF	JG
1.5	30	1	0	1	0.07	1	9	9	9	8	8	100
2	22	1	0	1	0.01	1	19	9	9	7	7	100
3	0	1	0	1	0.0022	1	39	9	9	7	7	200
4	0	1	0	1	0.0001	1	78	9	9	9	9	200

improvement of computer capability allows numerical calculations to be performed for Eq. (8) containing a constant value, Q_0, representing a complicated function of θ'. In the previous work [12–14], the term to cancel out θ' was added in Eq. (8). Inevitably, even the calculated curves of $2\pi q_j(\cos\theta_j)$ to give the best fit to the duller experimental curves for polyethylene [12, 14] and nylon 6 [13] spherulites were obliged to take large negative values at most polar angles, θ_j.

Returning to Fig. 5, the calculated curves are in fairly good agreement with the observed ones in the case of $\lambda = 1.5$. At $\lambda = 1.5$, the curve calculated for the (004) plane shows good agreement with the experimental result but the overlapped curve calculated was in poor agreement with the experimental result notwithstanding the appearance of a peak around 60°. Incidentally, small oscillations of the full curves at $\lambda = 4$ showing negative parts of $2\pi q_j(\cos\theta_j)$ are due to the procedure of expanding each sharp distribution function into an infinite series of spherical harmonics. Certainly, this is an expected deficiency of this method. However, small oscillations of the calculated curves were not observed for the films with a draw ratio less than 3.

As listed in Table 5, the effect of σ_1 is zero at all draw ratios. This means that the rotation of the rod around its own axis only occurs to ensure the preferential orientation of the V_1 axis (thickness direction of rod) perpendicular to the plane (0-X_3V_3 plane) containing a stretching direction and a rod axis. It should be noted that at $\lambda = 1.5$ and 2, Eq. (6) has a maximum value at $\theta_0 = 30°$ and 22°, respectively, indicating that most of the rods orient at a particular tilt angle θ_0 with respect to the stretching direction. Although these values of θ_0 were determined by the simplex method [32], these values at each draw ratio were in good agreement with the orientations of rods observed under optical microscopy (crossed polarization). Beyond $\lambda > 3$, the best fit was realized at $\theta_0 = 0°$, indicating the preferential orientation of rods with respect to the stretching direction. This preferential orientation was also confirmed by optical microscopy (crossed polarization). Another interesting phenomenon is the orientation of the crystallites within a rod. Judging from the small values of σ_3 at each draw ratio, the orientation of the crystallites within the rod is very small in spite of an increase in the draw ratio. This means that most of the crystallites are fixed within the rod and that the preferential orientation of the crystallites with respect to the stretching direction is mainly dependent upon the orientation of the rod.

On the basis of this model, small-angle light scattering from oriented rods is formulated. The intensity distribution of scattered light is discussed chiefly for Hv polarization conditions. Similar treatment was done for polyethylene [33] and nylon 6 [13] films with a deformed three-dimensional spherulite but no estimation using a similar method has ever been reported for rods as discussed before. In the model system needed for theoretical calculations, the rod is assumed to be finite in length but infinitesimally thin in thickness and transverse direction. To avoid extremely complicated treatments, the optical axis within the rod is assumed to be equivalent to the *c*-axis by neglecting scattering from amorphous chain segments.

The scattered intensity from an oriented rod may be given by

$$I(\theta,\mu) = \int_0^{2\pi}\int_0^{2\pi}\int_0^{\pi} \omega(\theta',\eta')[E(\theta,\mu)]^2 \sin\theta' \, d\theta' \, d\phi' \, d\eta' \tag{16}$$

where the angles θ and μ are the scattering and azimuthal angles. The amplitude, E, of the scattered ray is given by

$$E(\theta,\mu) = E_0 \int_{-L/2}^{L/2} (\mathbf{M}\cdot\mathbf{O}) \cos[k(\mathbf{r}\cdot\mathbf{s})] dr \ , \tag{17}$$

where L is the length of the rod and k denotes $2\pi/\lambda'$; λ' is the wavelength of the light within the specimen. $(\mathbf{M}\cdot\mathrm{O})$ in Eq.(17) is given by [13, 30]

$$(\mathbf{M}\cdot\mathbf{O}) = \int_0^{2\pi}\int_0^{\pi} (\alpha_3-\alpha_1)(\mathbf{U}_3\cdot\mathbf{X}_3)(\mathbf{U}_3\cdot\mathbf{X}_2) \left(\int_0^{2\pi} q(\alpha,\beta,\gamma)d\gamma\right) \sin\beta \, d\beta \, d\alpha \ , \tag{18}$$

where $(\mathbf{M}\cdot\mathrm{O})$ is the scaler product of the induced dipole moment, **M**, of the scattering element and the unit vector, **O**, along the polarization direction of the analyzer; **r** is the position vector along the rod axis; **s** is the vector defined by $(\mathbf{s}_0 - \mathbf{s}')$, where $\mathbf{s}_0$ and $\mathbf{s}'$ are unit vectors parallel to the propagation directions of the incident and scattered beams, respectively; $\mathbf{U}_3$ is the vector along the optical axis (the *c*-axis); $\mathbf{X}_3$ and $\mathbf{X}_2$ are the vectors along the X_3 and X_2 direction, respectively. α_3 and α_1 (or α_2) are the polarizabilities of the scattering element parallel and perpendicular to the principal optical axis, respectively. The detailed derivation is too much to be written explicitly. The scattered intensity distribution was calculated as a function of θ and μ. L/λ' is taken as 40. Before the numerical calculation to evaluate the scattered intensity, it should be noted that the intensity in Eq. (16) was normalized by L^2 because the length of each rod is related to the absolute intensity but not to the profile of the intensity distribution function.

The theoretical results from Hv scattering from rods oriented at desired draw ratios are shown in Fig. 6. At $\lambda = 1$, the shape of the pattern shows X-type scattering from the rods, the optical axes being oriented parallel with respect to the rod axis. Judging from Eq. (17), in the undrawn state this angular dependence with maximum intensity at odd multiplies of $\mu = 45°$ is reasonable but it is quite different from the observed pattern showing an indistinct circular type. The present model concerning only the orientation of rods with draw ratio has a defect. Accordingly, the calculated pattern is in good agreement with the observed one at $\lambda = 4$. The calculated pattern, however, cannot explain the growth of rods under the drawing process. Namely, the calculated patterns do not explain the continuous development of a clear type pattern from an indistinct circular pattern by oriented crystallization. To explain the drastic change of the pattern, the growth of rods by elongation must be taken into account in terms of kinetic theory but the introduction of this effect is too difficult to formulate. Apart from this discussion, the circular pattern of the undrawn film could be easily obtained by taking values of L/λ' lower than unity in stead of $L/\lambda' = 40$. This treatment satisfies the system composed of a random array of crystallites that are small compared with the wavelength of light within the undrawn specimen and can explain qualitatively the change in the pattern by an increase in rod length under the elongation process. The circular-type pattern could be obtained at $L/\lambda' < 1$, although the pattern is not shown here.

Detailed observation reveals that the scattering lobes in the calculated pattern are extended gradually in the horizontal direction with increasing draw ratio, indicating the preferential orientation of rods with respect to the stretching direction. The theoretical treatment is certainly effective to explain the four-leaf pattern but cannot explain the superposition of a four-leaf pattern and sharp streaks in the horizontal direction at $\lambda = 1.5$–3. Following Matsuo et al. [29, 30] the sharp streaks obviously reflect interparticle interference effects of the rods and the theoretical treatment must be taken into consideration.

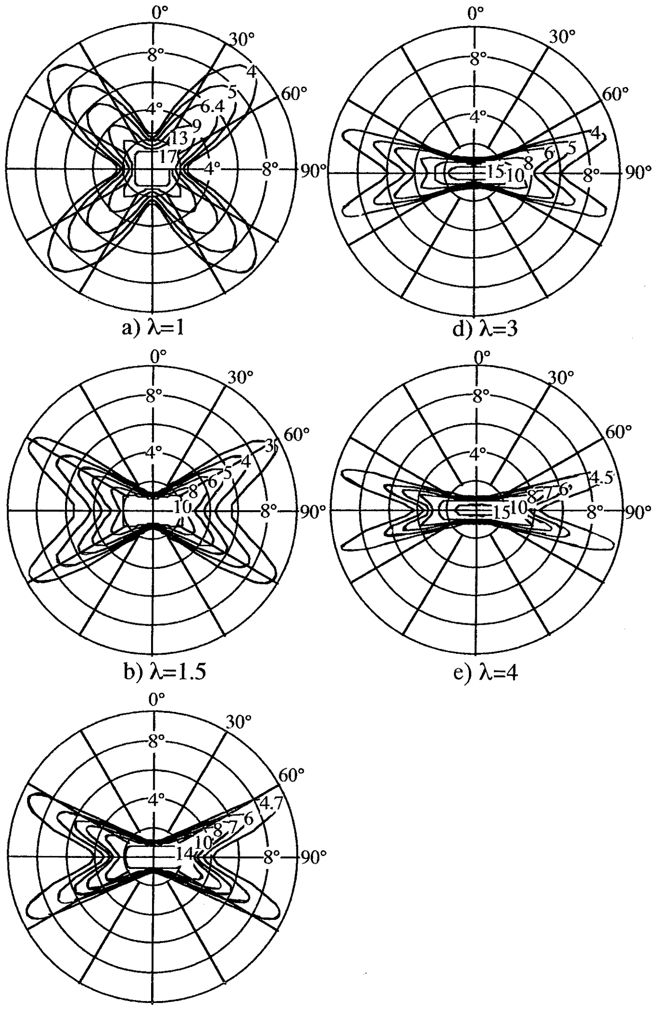

a) λ=1
d) λ=3
b) λ=1.5
e) λ=4
c)λ=2

Fig. 6a–e Hv light scattering patterns calculated using Eqs. (18), (19) and (20)

In order to obtain more conclusive evidence for interparticle interference effects of the rods, we refer to the model system shown in Fig. 7. In this model system, the centers of gravity of the *j*th and $(j+1)$th rods with three-dimensional orientation are situated in the two-dimensional plane $0\text{-}X_3X_2$ and φ denotes the angle between the X_3 axis and the axis to link the *j*th rod with the $(j+1)$th rod. The distance between the centers of gravity is given by X_i. Effort has been made to preserve the notation of Blundell [34, 35] in order to emphasize the similarity of formation between small-angle light and X-ray scattering.

Considering the geometrical arrangement of the rods in Fig. 7, the scattering amplitude E_j from the *j*th rod, whose center of gravity is situated at a distance U_j from the center of the coordinate system is given by

$$E_j = \int_s (\mathbf{M}\cdot\mathbf{O})\exp[-2\pi i(\mathbf{s}\cdot\mathbf{r}_j)]\mathrm{d}S \ . \tag{19}$$

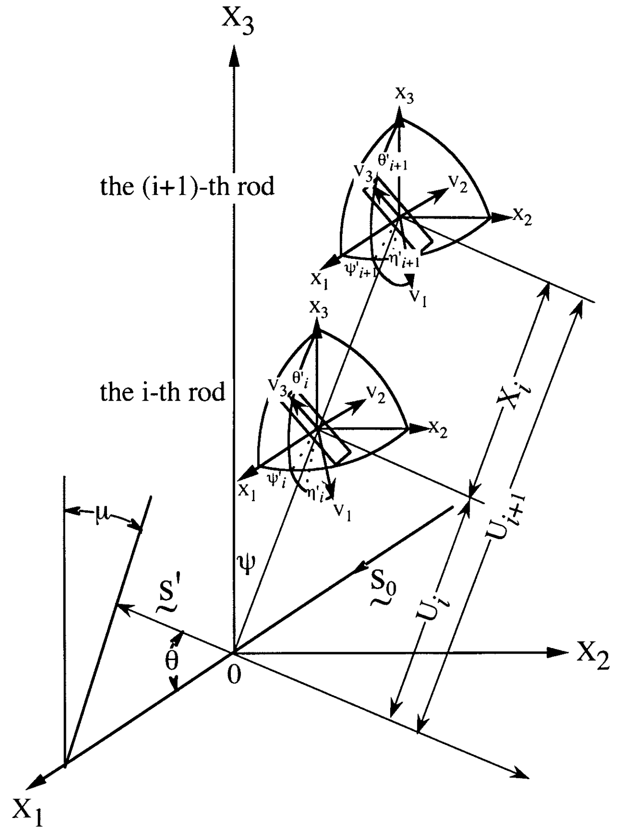

Fig. 7 A model used for the theoretical analysis of light scattering intensity distribution from the assembly of rods

According to the method proposed by Blundell [34, 35] the normalized scattered intensity from an assembly of N rods is $\sum_{i=1}^{N}\sum_{j=1}^{N} E_iE_j^*/N$. E_j^* denotes the complex conjugate of E_j and $\mathbf{r}_j$ is the position vector of a scattering element situated at a distance of $\mathbf{r}_j$ from the center of the coordinate system $0\text{-}X_1X_2X_3$. The fluctuations of rod length and angle ψ are neglected. As the result,

$$I_t = \frac{1}{N}\sum_{i=1}^{N}\sum_{j=1}^{N} E_iE_j^* = I_B - I_C \ , \tag{20}$$

where I_B and I_C in the real part are given by

$$I_B = Re\left[\frac{I(1+F_X)}{1-F_X}\right] \ , \tag{21}$$

$$I_C = Re\left[\frac{2I(1-F_X^N)}{N(1-F_X)^2}\right] \ , \tag{22}$$

where

$$F_X = \int_{-\infty}^{\infty} H(X_j)\exp(-2\pi i b X_j)\mathrm{d}X_j \tag{23}$$

and

$$b = \sin\theta \cos\mu/\lambda' \ . \tag{24}$$

The term I_B is mainly responsible for the first- and higher-order diffraction peaks and the term I_C gives the zero scatter. The term I in I_B and I_C corresponds to the scattered intensity from a rod which is given as Eq. (16). In the present model system, the term of diffuse scattering does not include in I_B and only contains the term $Re(1+F_X)/(1-F_X)$ corresponding to the lattice factor, which converges to unity as the scattering angle θ increase. X_j in Eq. (23) is given by the following symmetric function with the respective mean length $\overline{X}$ and the standard deviation σ_X; thus

$$H(X_j) = \frac{1}{\sqrt{2\pi\sigma_X^2}} \exp\left[\frac{-(X_j - \overline{X})^2}{2\sigma_X^2}\right] \ . \tag{25}$$

Equation (25) is associated with the distance statistics introduced by Hosemann and Bagchi [36]. When $\sigma_X = 0$, the displacement between the two adjacent rods is the same distance and with increasing σ_X, the fluctuation of displacement increases. In the present system, $\sigma_X/\overline{X}$ is fixed to be 0.01 to ensure the small fluctuation.

In a real system, the position of the specimen sampled by the laser beam contains a distribution of the number of rods, N. This concept must be introduced in order to smear out the many subsidiary maxima that appear at lower scattering angles. This has been taken into consideration by Hashimoto et al. [37], who introduced a discrete symmetrical distribution of N with standard deviation $\sigma_N = 3$ to calculate the small-angle X-ray intensity. This distribution is written as

$$P(N) = \exp\left(-\frac{(N-\overline{N})^2}{2\sigma_X^2}\right) \Bigg/ \sum_{N=1}^{2\overline{N}-1} \exp\left(-\frac{(N-\overline{N})^2}{2\sigma_X^2}\right) \ . \tag{26}$$

In the present work, we assume the same type of distribution of N. Then, the average value of the term I_c is given by

$$\langle I_C \rangle = \sum_{N=1}^{2\bar{N}-1} I_C P(N) \ . \tag{27}$$

Let us consider the μ dependence of the scattered intensity distribution. Figures 8 and 9 show the patterns calculated at $\lambda = 1.5$ and 2 as a function of $L/\overline{X}$ $(=q)$, in

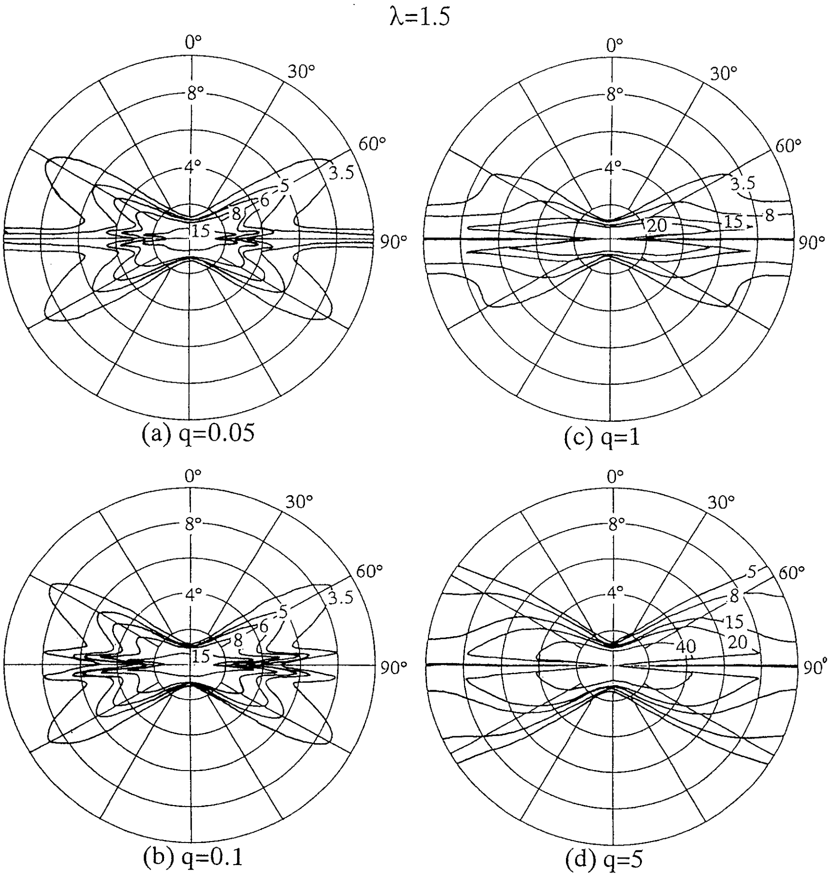

(a) q=0.05
(c) q=1
(b) q=0.1
(d) q=5

Fig. 8a–d Light scattering patterns from the film with $\lambda = 1.5$ calculated with a change in $q(=L/X)$ on the basis of the model in Fig. 7

Fig. 9a–d Light scattering patterns from the film with $\lambda = 2$ calculated with change in $q(=L/X)$ on the basis of the model in Fig. 7

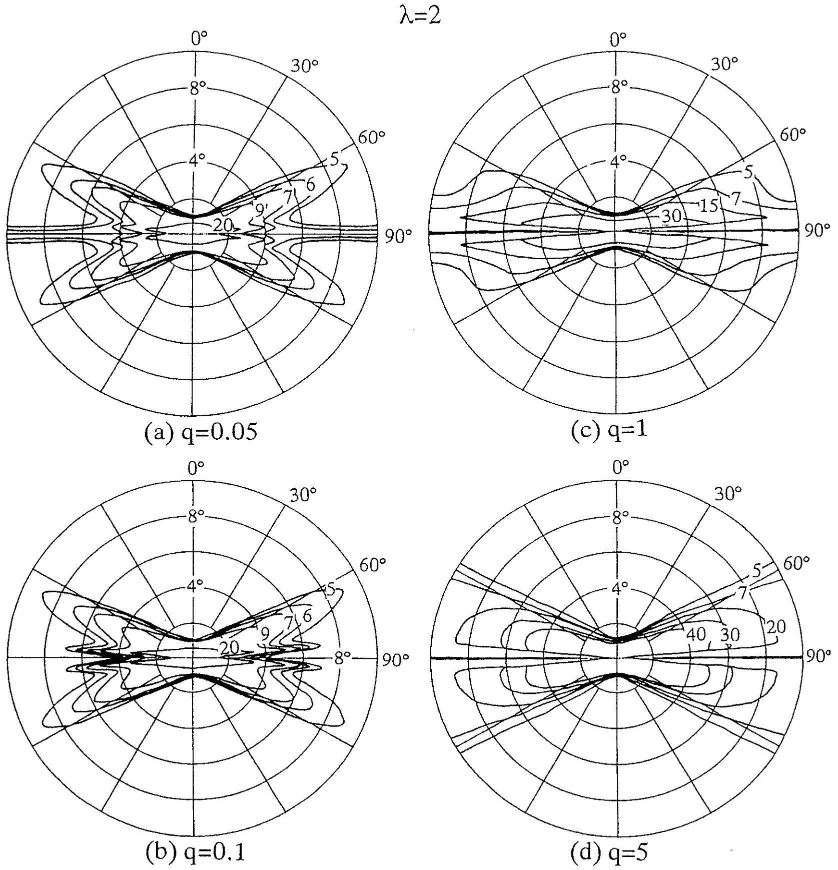

which the value of ψ was set to be zero in an attempt to realize the appearance of streaks in the horizontal direction. The sharp streaks were superposed in addition to the four-leaf pattern in Fig. 8. Thus, it is evident that the streaks reflect an interparticle interference effect of the rods. At lower scattering angles of θ, the four sharp streaks appeared around at $\mu = \pm 5°$ and $\mu = \pm 175°$ and the streaks extended remarkably in the horizontal direction with increasing θ. At $q = 0.05$, denoting the system where the distance connecting each center of two rods is much longer than the rod length, the scattering pattern shows a clear profile. An increase in q, i.e., a decrease in $\overline{X}$, causes the pattern to be dulled. Namely, the increase in q associated with interparticle interference effects of the rods causes a significant effect on not only the streaks but also on the four-leaf lobes. The best fit between the calculated and observed patterns can be realized by choosing a suitable value of q. Namely, the pattern (c) with $q = 1°$ at $\lambda = 1.5$ and the pattern (a) with $q = 0.05$ at $\lambda = 2$ are in good agreement with the observed ones at $\lambda = 1.5$ and $\lambda = 2$ in Fig. 4, respectively. The appearance and the disappearance of the streaks under drawing of the film correspond to the appearance of the assembly of rods with ordered orientation by the initial elongation and the disruption of the assembly by further elongation, respectively. Under optical microscopy (cross-polarization), this phenomenon was confirmed as the appearance and the disappearance of network structures.

A series of calculations for polarized light scattering takes account only of the crystalline orientation within the oriented rod and omits contributions from other factors such as orientation and density fluctuation of the crystals, size distribution of rods, noncrystalline orientation effects including the anisotropy of the surrounding medium and birefringence effects. The effect of the orientation distribution of noncrystalline chain segments within the rod is perhaps the most significant factor among their unknown contributions and must be taken into account in further studies.

Conclusion

The influence of the applied stress on the thermal reversibility of ETFE was examined by X-ray diffraction. The lattice space of the (*hk*0) plane was expanded as temperature increased and returned to normal size in the cooling process. Under the external applied stress, the dimensional change in the lattice space in the heating and cooling processes was indeed irreversible. Moreover, the space did not return to normal size, even when the stress was removed after the heat treatment. The small change in the X-ray diffraction patterns is attributed to the change in temperature but is hardly affected by the applied stress. The Hv light scattering from oriented films displayed the superposition of a broadleaf pattern and a sharp pattern of streaks. This indicates the existence of the oriented rod and the interparticle interference effect of the rods. This deformation mechanism was discussed in relation to the orientation of crystallites within the rod by using a proposed model. In this model, the orientation function of the crystallites was assumed to be a function of rod orientation. On the basis of the orthorhombic crystal unit proposed by Tanigami et al., the orientation functions of the reciprocal lattice vector were obtained from the orientation functions of rods and crystallites containing 12 parameters. The calculated results were in fairly good agreement with the observed ones by choosing suitable values of the parameters. On the basis of both functions determined with suitable values of the parameters, Hv light scattering was formulated by introducing interparticle interference effects of the rods. The calculated patterns were in good agreement with the observed ones with a proper choice of the ratio of the length of the rod and the distance between the centers of gravity of the rods.

References

1. Wilson FC, Starkweather HW Jr (1973) J Polym Sci Polym Phys Ed 11:919
2. Tanigami T, Yamaura K, Matsuzawa S, Ishikawa M, Mizoguchi K, Miyasaka K (1986) Polymer 27:999
3. Tanigami T, Yamaura K, Matsuzawa S, Ishikawa M, Mizoguchi K, Miyasaka K (1986) Polymer 27:1521
4. Scheerer K, Wilke W (1987) Colloid Polym Sci 265:206
5. Iuliano M, De Rosa C, Guerra G, Petraccone V, Corradini P (1989) Makromol Chem 190:827
6. Guerra G, De Rosa C, Iuliano M, Petraccone V, Corradini P (1993) Makromol Chem 194:389
7. D'Aniello C, De Rosa C, Guerra G, Petraccone V, Corradini P, Ajroldi G (1995) Polymer 36:967
8. Radice S, Del Fanti N, Zerbi G (1997) Polymer 38:2753
9. Petraccone V, De Rosa C, Guerra G, Iuliano M, Corradini P (1992) 33:22
10. De Rosa C, Guerra G, D'Aniello C, Petraccone V, Corradini P, Ajroldi G (1995) J Appl Polm Sci 56:271
11. Pieper T, Heise B, Wilke W (1989) 30:1768
12. Nomura S, Matsuo M, Kawai H (1972) J Polym Sci Polym Phys Ed 10:2489
13. Matsuo M, Nomura S, Kawai H (1976) J Polym Sci Polym Phys Ed 14:223
14. Matsuo M, Hirota K, Hujita K, Kawai H (1978) Macromolecules 11:1000
15. Sawatari C, Iida M, Matsuo M (1984) Macromolecules 17:1765
16. Matsuo M, Yanagida N (1991) Polymer 32:2561
17. Roe RJ, Krigbaum WR (1964) J Chem Phys 40:2608
18. Krigbaum WR, Roe RJ (1964) J Chem Phys 41:737
19. Guerra G, De Rosa G, Iuliano M, Petraccone V, Corradini P (1993) Macromol Chem 194:389
20. Starkweather HW Jr (1973) J Polym Sci Polym Phys Ed 11:587
21. Nishimura H, Yamabe M (1974) Rep Les Lab Asahi Glass Co Ltd 24:59
22. Raff RAV (1967) In: Mark HF, et al (eds) Encyclopedia of polymer science and technology, vol 6. Wiley, New York, pp 275–332
23. Nakayasu H, Markovitz H, Plazek DJ (1961) Trans Soc Rheol 5:261
24. Takayanagi M, Matsuo M (1967) Macromol Sci Phys B 1:407
25. Tsuge K, Enjoji H, Terada H, Ozawa Y, Wada Y (1962) Jpn J Appl Phys 1:270
26. Iwayanagi S, Miura I (1965) Jpn J Appl Phys 4:94
27. Stein RS, Rhodes MB (1960) J Appl Phys 31:1873
28. Rhodes MB, Stein RS (1969) J Polym Sci Part A-2 7:1539
29. Matsuo M, Tamada M, Terada T, Sawatari C, Niwa M (1982) Macromolecules 15:988
30. Nomura S, Asanuma A, Suehiro S, Kawai H (1971) J Polym Sci Part A-2 9:1991
31. Matsuo M, Nomura S, Kawai H (1973) J Polym Sci Part A-2 11:2057
32. Spendly W, Hext GR, Himsworth FR (1968) Technometrics 4:441
33. Nomura S, Matsuo M, Kawai H (1974) J Polym Sci Part A-2 12:1371
34. Blundell D (1970) J Acta Crystallogr Sect A 26:472
35. Blundell D (1970) J Acta Crystallogr Sect A 26:476
36. Hosemann R, Bagchi SN (1962) Direct analysis of diffraction by matter. North-Holland, Amsterdam
37. Hashimoto T, Nagatoshi K, Toda A, Hasegawa H, Kawai H (1974) Macromolecules 7:264